Electronic Supporting Information

Hybrid photocathode based on Ni molecular catalyst and Sb₂Se₃ for solar H₂ production

D. Alicia Garcia-Osorio,[a] Thomas P. Shalvey,[a] Liam Banerji,[a] Khezar Saeed,[a,b] Gaia Neri,[a,c] Laurie J. Phillips,[a] Oliver S. Hutter,[a,d] Carla Casadevall,[e] Daniel Antón-García,[e] Erwin Reisner,[e] Jonathan D Major,[a*] Alexander J Cowan[a*]

[a] Stephenson Institute for Renewable Energy, University of Liverpool, L69 7ZF, UK.

[b] Current address Department of Chemistry, Aarhus University, 8000 Aarhus C, Denmark.

[c] Current address Enapter S.R.L, via di Lavoria 56/g, 56040 Pisa.

[d] Department of Mathematics, Physics and Electrical Engineering, Northumbria University, NE1 8ST, UK

[e] Yusuf Hamied Department of Chemistry, University of Cambridge, CB2 1EW, UK.

Contents

1 Experimental details

1.1 Photocathode assembly Sb$_2$Se$_3$/CdS/TiO$_2$-*meso*/NiP

SnO$_2$:F (FTO) coated glass substrates (TEC15, NSG group) were cleaned in ultrasonic baths of Hellmanex III detergent (2%), DI water and isopropyl alcohol in sequence, before drying with compressed nitrogen. A 70 nm Au layer (99.95%, Advent RM) was then thermally evaporated at a rate of ~1 Å s^{-1}. The Sb$_2$Se$_3$ absorber layer was deposited by close spaced sublimation (CSS) in a two-step process, with a small grain seed layer initially deposited under vacuum with a substrate temperature of 350°C to improve uniformity.[1,2] This is followed by a higher temperature growth stage whereby the chamber is backfilled with 10 Torr N$_2$ and the substrate temperature is increased to 400°C to produce a ~1.5 μm thick film with a large grain size. RF magnetron sputtering was then used to deposit 20 nm CdS (60W, 5mTorr Ar, T$_{sub}$=200°C) and 100 nm TiO$_2$ (150W, 3mTorr Ar, T$_{sub}$=25°C) layers from 3" diameter compound targets.

1.2 TiO$_2$ mesoporous layer preparation

The method for preparation of TiO$_2$ mesoporous (TiO$_2$-*meso*) layer was initially optimized on FTO glass (TEC-15) cleaned in acetone, ethanol, DI water for 20 min each in an ultrasonic bath. Greatcell Solar® 18NR-T Titania Paste was slot coated using a glass pipette and Scotch® Magic™ Tape as template. To remove the organic binder present in the Titania paste, the films were UV cured using a 365 nm UV LED (2.9 W, 2.2 mm x 2.2 mm, LZ4-04UV00/ LED Engin) for 68 h was required, figure S5. The TiO$_2$-*meso* layer was then sintered at 350 °C under constant N$_2$ flow for 1 h with the final sample labelled as TiO$_2$-*meso*(UV). Profilometry measurements indicate that the UV cured film is *ca.* 4-6 μm thick. To compare the behaviour of the UV cured films to those prepared by a conventional thermal method, TiO$_2$ paste was deposited on FTO in the same manner and then annealed at 450 °C under air during 1 h. Those samples were label as TiO$_2$-*meso*(450°C, air). Once the TiO$_2$ mesoporous layer deposition made by UV curing was optimized, the same protocol was applied on the top of FTO/Au/Sb$_2$Se$_3$/CdS/TiO$_2$ photoelectrodes. We labelled those samples as Sb$_2$Se$_3$/CdS/TiO$_2$-*meso*.

The **NiP** molecular catalyst was synthesized using previously described methods.[3-6] **NiP** immobilization was achieved by socking the samples in a 0.5 mM **NiP** solution prepared using dry methanol overnight (16 h) in the dark. Photoelectrodes were then rinsed thoroughly in dry methanol to remove the **NiP** excess not bound to the TiO$_2$, followed by vacuum dried process at 60 °C for 2 hr in the dark to remove methanol. The same experimental protocol was followed for the **NiP** immobilization in all the samples studied: planar device (Sb$_2$Se$_3$/CdS/TiO$_2$), the complete high surface area photoelectrode (Sb$_2$Se$_3$/CdS/TiO$_2$-*meso*), and the bare TiO$_2$-*meso* (without the Sb$_2$Se$_3$ underneath) for the control experiments.

To determine the **NiP** loading, the photoelectrodes were soaked in 2 mL of 0.1 M NaOH for 1 h. The resultant **NiP** solution was studied using UV/Vis spectroscopy (Shimadzu 2300) and the concentration calculated by measuring the absorbance at 254 nm and through the use of a calibration curve made with known concentrations of **NiP** in 0.1 M NaOH.

1.3 Photoelectrodes characterization

Film thicknesses were measured ex situ using an Ambios XP-200 profilometer. Transmission and reflectance measurements were taken between 250-1500 nm using a Shimadzu SolidSpec-3700 UV-vis-NIR spectrophotometer in order to calculate the absorption coefficient, which was then used to estimate the band gap for CdS, Sb$_2$Se$_3$ and TiO$_2$ thin films according to the Tauc method.[7]

SEM and elemental analysis were taken on a Hitachi S4800 cold field emission gun (FEG) microscope detecting secondary electrons in the in-column detector. A working distance of 8 mm was used for all imaging. Voltage and gun current were set to 5 kV and 7 µA respectively. Elemental analysis by SEM-EDX was carried out on the same samples using the same Hitachi S4800 microscope, with an Oxford Instruments AztecOne attachment with a 10 mm^2 silicon drift detector (SDD). A working distance of 15 mm was used for all elemental analysis. A voltage of 20 kV was selected based on the Kα transition energies for Pt and Ni (Pt Lα = 9.441 keV, Ni Kα = 7.471 keV). Gun current was set to 15 µA. The analysis was taken with the aperture completely removed to achieve maximum count rate whilst maintaining dead time <45%.

XPS data collection was performed at the EPSRC National Facility for XPS ('HarwellXPS'), operated by Cardiff University and UCL, under contract No. PR16195. XPS data was acquired using a Kratos Axis SUPRA using monochromated Al kα (1486.69 eV) X-rays at 12 mA emission and 12 kV HT (144W) and a spot size/analysis area of 700 x 300 µm. The instrument was calibrated to gold metal Au 4f (83.95 eV) and dispersion adjusted give a BE of 932.6 eV for the Cu 2p3/2 line of metallic copper. Ag 3d5/2 line FWHM at 10 eV pass energy was 0.544 eV. Source resolution for monochromatic Al Kα X-rays is ~0.3 eV. The instrumental resolution was determined to be 0.29 eV at 10 eV pass energy using the Fermi edge of the valence band for metallic silver. Resolution with charge compensation system on <1.33 eV FWHM on PTFE. High resolution spectra were obtained using a pass energy of 20 eV, step size of 0.1 eV and sweep time of 60s, resulting in a line width of 0.696 eV for Au 4f7/2. Survey spectra were obtained using a pass energy of 160 eV. Charge neutralisation was achieved using an electron flood gun with filament current = 0.38 A, charge balance = 2 V, filament bias = 4.2 V. Successful neutralisation was adjudged by analysing the C 1s region wherein a sharp peak with no lower BE structure was obtained. Spectra have been charge corrected to the main line of the carbon 1s spectrum (adventitious carbon) set to 284.8 eV. All data was recorded at a base pressure of below 9 x 10^{-9} Torr and a room temperature of 294 K.

Raman analysis was carried out using a Raman microscope (Renishaw InVia) with a 50x objective (Leica). Before measurements, Raman band positions were calibrated *vs* the 520 cm^{-1} silicon peak with a resolution of 1 cm^{-1}. A 532 nm green laser was used with 0.5% laser intensity for 60 s on Sb$_2$Se$_3$/CdS/TiO$_2$-*meso* and 5% laser intensity for 60 s for the sample without the TiO$_2$-*meso* layer (Sb$_2$Se$_3$/CdS/TiO$_2$). The same conditions were used pre, post N$_2$ annealing and post Controlled Potential Photoelectrolysis (CPP). To determine the effect of the N$_2$ annealing on the crystalline structure of the TiO$_2$ layer made RF magnetron sputtering 15% laser intensity was used for 60 s.

1.4 Photoelectrochemical measurements

A three-electrode cell was used for all the electrochemical measurements. Sb$_2$Se$_3$/CdS/TiO$_2$(-*meso*/**NiP**) was the working electrode, a Pt mesh was the counter electrode and Ag/AgCl (3 M NaCl) the reference electrode. The electrolyte was 0.1 M Na$_2$SO$_4$, pH 3 (adjusted with acetic acid) in Milli-Q water (18.2 MΩ·cm) and a customised electrochemical cell was purged with N$_2$ for 25 min before each electrochemical test, figure S1.1. The pH 3 was chosen considering the highest catalytic activity of **NiP** towards H$_2$ production after being immobilised on TiO$_2$. It has been found that at lower (2) and higher (4) pH's the rate of hydrogen production decreased by > 50% and as well as the Faradic Efficiency.[8]

Electrochemical measurements were carried out using a PalmSens3 potentiostat. Linear sweep voltammetry (LSV) was conducted at 10 mV s^{-1} from the open circuit potential in the cathodic direction. The electrochemical potentials were converted to the RHE according to Eq. (1)[9]

$$E \ (vs \ RHE) = E \ (V \ vs \ Ag/AgCl) + 0.059 * pH + 0.209 \qquad \text{(Eq. 1)}$$
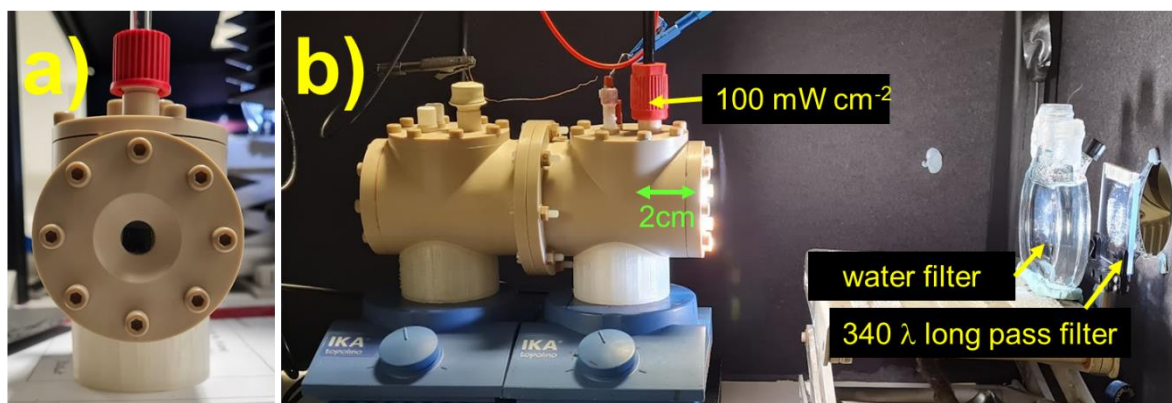
Figure S1.1 Customized photoelectrochemical cell used for the Controlled Potential Photoelectrolysis (CPP).

The light source was a Xe lamp providing an irradiation of 100 mW cm^{-2} (300 W Xe lamp, LOT Quantum Design) at the front of the electrochemical cell. Schott glass long pass filters were used to limit the output to $\lambda \geq 340$ nm and a water filter removed the infrared component, and a neutral density filter was used to decrease to drop the light intensity to 20 mW cm^{-2} Photoelectrodes were front illuminated across a quartz window. Controlled potential photoelectrolysis (CPP) tests were carried out in a gas tight customised H cell at 0 V *vs* RHE with a Nafion membrane (N117) between the anode and cathode, for these experiments the electrochemical cell was purged for 30 min with N_2 and 1% CH_4 as an internal standard for gas chromatography. Gas compositions were determined using an Agilent 6890N instrument with helium N6 (BOC) as the carrier gas (5 mol min^{-1}), equipped with a 5 Å molecular sieve column (ValcoPLOT, 30 m length, 0.53 mm ID) and a pulsed discharge detector (D-3-I-HP, Valco Vici).

Pt was photoelectrodeposited according to previous studies[9] by applying a constant current of -30 µA cm^{-2} for 15 min under light irradiation of 100 mW cm^{-2}, $\lambda \geq 340$ nm and a water filter, in a solution containing 1 mM H_2PtCl_6 and 0.1 M Na_2SO_4.

IPCE measurements were carried out using 100 W tungsten lamp as a light source coupled with a monochromator (OBB Corp., typically set to 4 nm resolution). The light intensity was measured with a Si-photodiode detector (S120VC) and the IPCE was calculated using

$$IPCE\ (\%) = \frac{1240 * J}{\lambda * P} \qquad \text{Eq (2)}$$

Where J is the photocurrent density (mA cm^{-2}) and P is the light power density (mW cm^{-2}) at each wavelength (λ). The IPCE spectra was collected at 0 V *vs* NHE.

2. Supporting figures

2.1. Band Gap (E_g) of the different semiconductors in the device
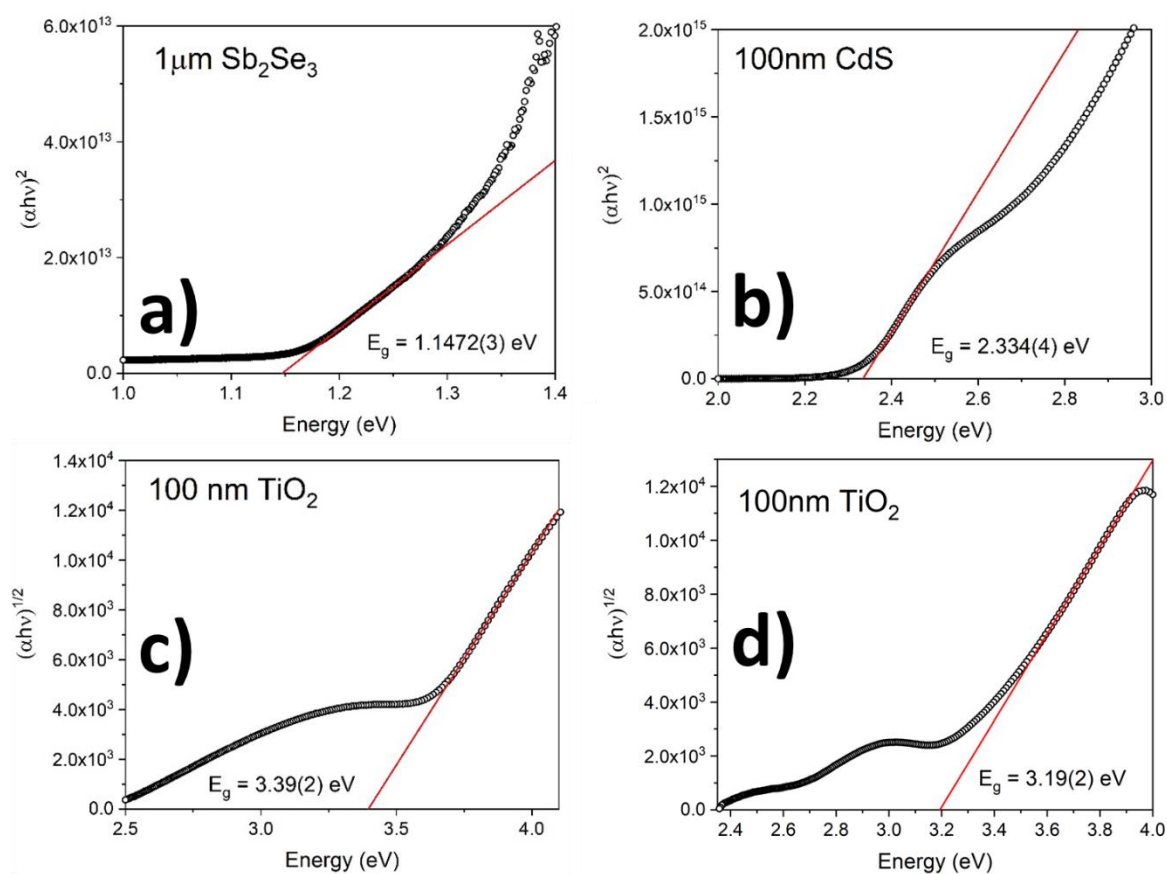

Figure S2.1. Tauc plots of (a) Sb_2Se_3, (b) CdS, (c) TiO_2 fresh-made by RF magnetron sputtering, and (d) TiO_2 after N_2 annealing at 350 °C
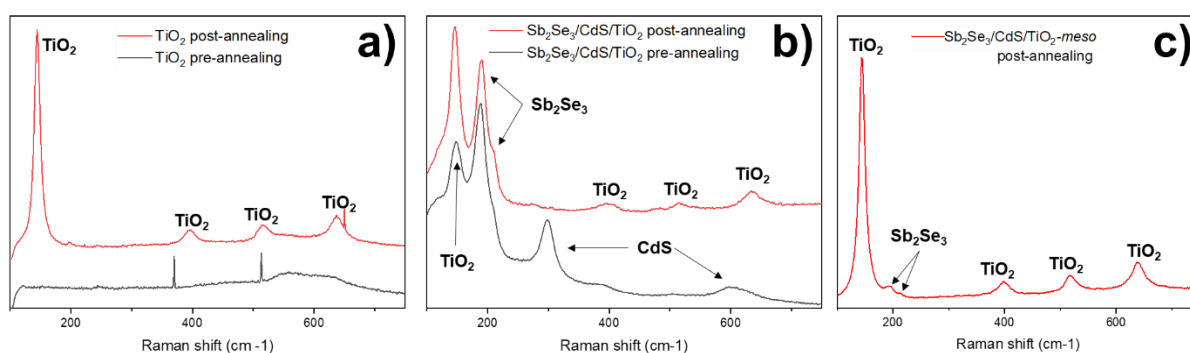
2.2. Raman analysis pre/post heat treatment

Figure S2.2. Raman spectra pre (black trace) and post (red trace) N_2 annealing at 350 °C of (a) sputtered TiO_2 on FTO. Following annealing of the sputtered TiO_2, Raman modes assignable to anatase TiO_2 were found. (b) $Sb_2Se_3/CdS/TiO_2$, and (c) $Sb_2Se_3/CdS/TiO_2$-*meso*.

2.3. SEM images before electrolysis
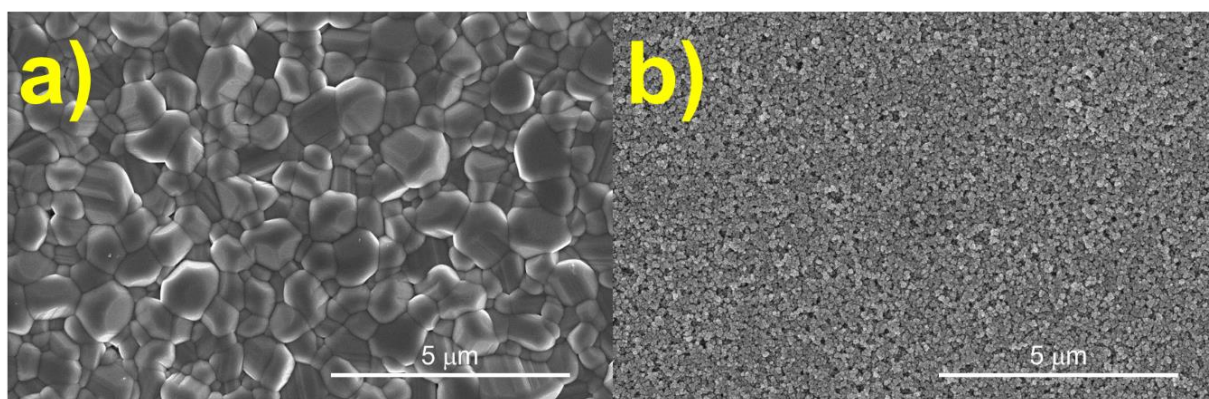
Figure S2.3 Top view SEM images of (a) $Sb_2Se_3/CdS/TiO_2$ and (b) $Sb_2Se_3/CdS/TiO_2$-*meso*.

2.4. LSV with no catalyst
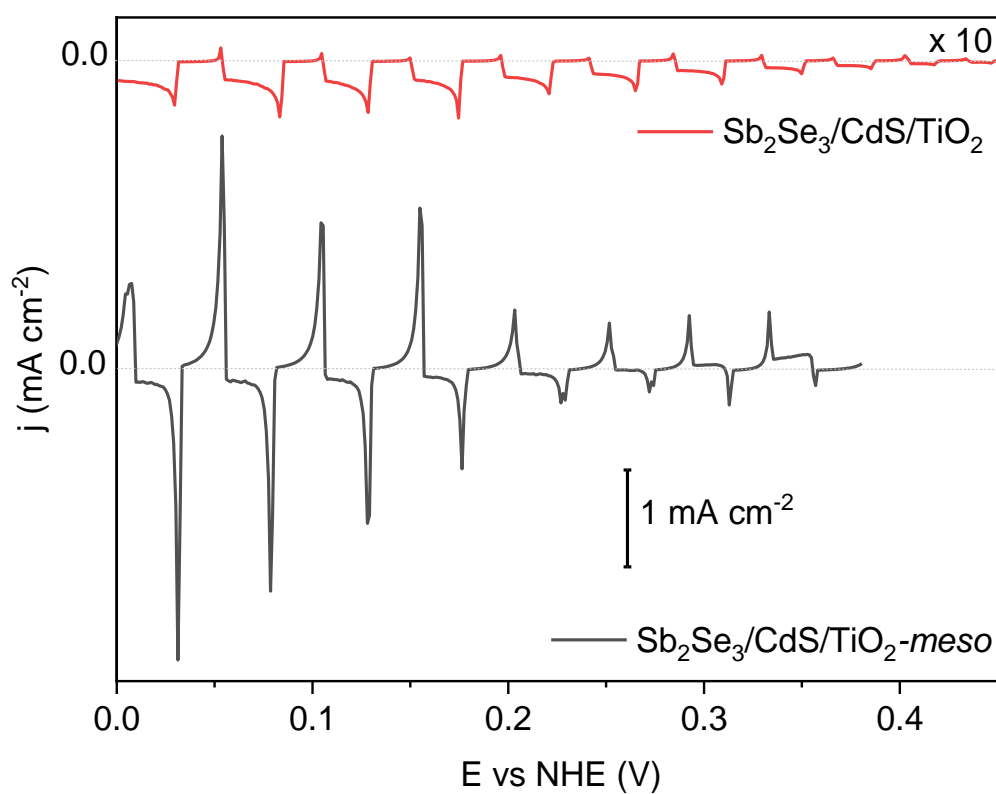
Figure S2.4: Light chopped LSV of $Sb_2Se_3/CdS/TiO_2$(-*meso*) without catalyst in 0.1 M Na_2SO_4 pH 3 at 100 mW cm^{-2} and $\lambda > 340$ nm.

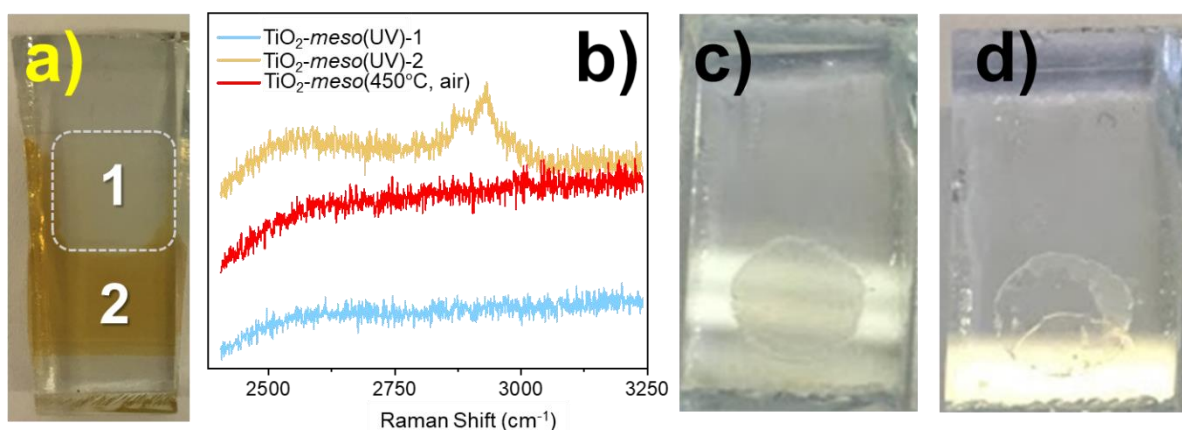## 2.5. Raman spectra of UV cured TiO$_2$-*meso* films

Figure S2.5 (a) TiO$_2$-*meso*(UV) electrode. Region 1 has been UV-cured for 68 hrs and the α-terpinol is visibly removed. Region 2 has not been UV cured. (b) Raman spectra of region 1 (blue trace) and 2 (yellow trace) from panel (a), showing the absence of ν(C-H) modes of α-terpinol[10] at 2870 and 2910 cm^{-1} following curing. A Raman spectra of TiO$_2$-*meso*(450°C, air shown as red trace) is also included as a control. TiO$_2$-*meso*(UV) (c) before and (d) after being immersed in 0.1 M Na$_2$SO$_4$ pH 3. It is notable that in image (d) TiO$_2$-*meso* layer delaminated following immersion in the electrolyte.

2.6. N$_2$ annealing of TiO$_2$-*meso*(UV)

To address the poor electrochemical properties and the low stabilities of the TiO$_2$-*meso*(UV) films in the electrolyte, samples were annealed under N$_2$ at 350 ºC for 60 min to increase TiO$_2$ particle interconnectivity and to aid substrate adhesion. Figure S2.6 compares the electrochemical response by cyclic voltammetry (a) and Electrochemical Impedance Spectroscopy (EIS, b) of TiO$_2$-*meso*(UV) and the control sample prepared by typical thermal annealing TiO$_2$-*meso*(450°C, air). Note that these electrochemical studies were carried out only with the mesoporous TiO$_2$ layer on FTO (without the underlying Sb$_2$Se$_3$/CdS/TiO$_2$-*sputtered* structure), for direct analysis of the annealing effect on the TiO$_2$-*meso*.
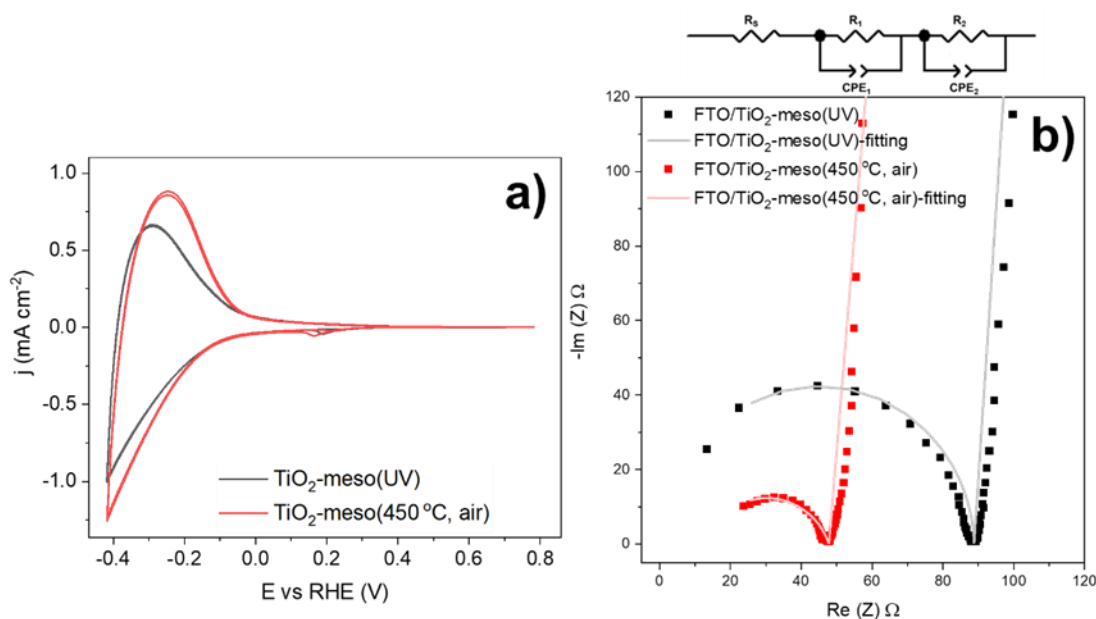

Figure S2.6 Comparison of the TiO$_2$-*meso* electrochemical properties made by UV curing followed by N$_2$ annealing at 350 ºC (black trace) and the control sample annealed at 450 ºC in air (red trace). (a) Cyclic voltammetry at 100 mV s^{-1}. (b) EIS spectra at 0 V *vs* RHE, with dots representing the experimental data and the fitted continuous line obtained using the equivalent circuit shown. Electrolyte: 0.1M Na$_2$SO$_4$ pH 3.

The N$_2$ annealing indeed aided the TiO$_2$ particle adhesion. However, the EIS analysis indicated the resistance of the TiO$_2$-*meso* film was higher for film made by UV curing than by the traditional air annealing process, being 87.2 and 35 Ω respectively.

Following annealing, **NiP** was immobilised on the TiO$_2$-*meso*(UV) and a control TiO$_2$-*meso*(450°C, air) sample. Figure S2.7a shows the cyclic voltammetry at 100 mV s^{-1} before and after the **NiP** immobilization on TiO$_2$-*meso*(UV) in 0.1M Na$_2$SO$_4$ pH 3, the bare TiO$_2$-*meso*(UV) displays the "trumpet shape" typically associated to the filling and emptying of the conduction band from the TiO$_2$. After the **NiP** immobilization, the oxidation current significantly diminishes indicating electron consumption by the molecular catalyst to produce H$_2$.[8] Figure S2.7b compares the chronoamperometry test using a TiO$_2$ mesoporous sample made by UV curing (TiO$_2$-*meso*(UV)/**NiP**) *vs* the common annealing process (TiO$_2$-*meso*(450°C, air)/**NiP**) after the catalyst immobilization at -0.25 V *vs* RHE in 0.1 M Na$_2$SO$_4$ pH 3. The electrochemical behaviour of both samples is similar with slightly lower current for the sample made by UV curing, presumably due to the higher film resistance, considering the similar catalyst loading (table S1).
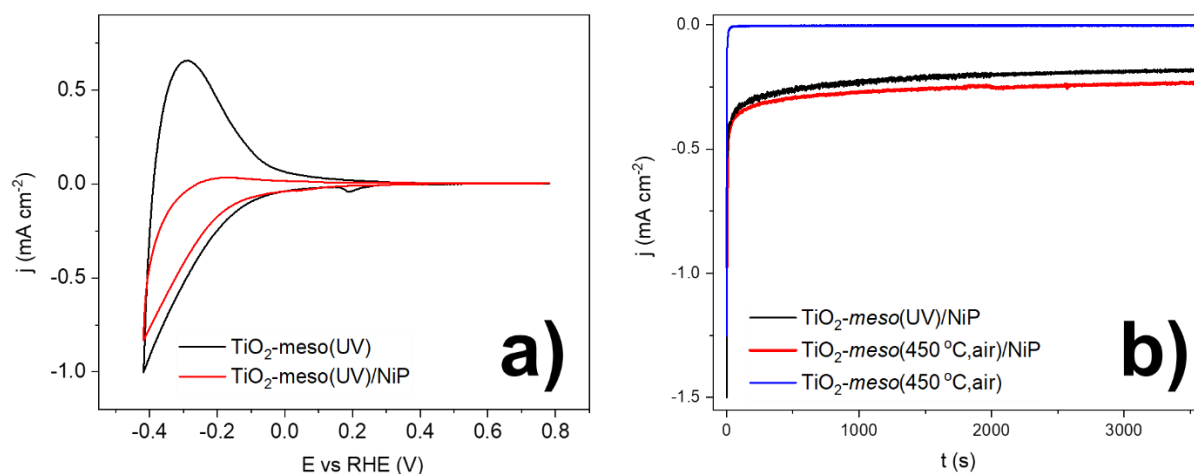
Figure S2.7. (a) Cyclic voltammetry before (black trace) and after the **NiP** immobilization (red trace) on TiO$_2$-*meso*(UV) in 0.1M Na$_2$SO$_4$ pH 3 at 100 mV s^{-1}. (b) Chronoamperometry test at -0.25 V *vs* RHE of TiO$_2$-*meso*/**NiP** with the TiO$_2$-*meso* layer made by air annealing (TiO$_2$-*meso*(450°C, air)/**NiP**), and by 68h UV curing followed by N$_2$ annealing at 350 °C (TiO$_2$-*meso*(UV)/**NiP**) in 0.1 M Na$_2$SO$_4$ pH 3. The control sample with no catalyst, made by the typical thermal annealing TiO$_2$-*meso*(450°C, air), showed low currents ~ -4 μA cm^{-2}.

It is worthy to notice that N$_2$ annealing without the prior UV curing does not produce films with suitable properties to be used as TiO$_2$ mesoporous scaffold. Figure S2.8 shows pictures of TiO$_2$-*meso* after N$_2$ annealing without prior UV curing at different temperatures: 234, 350 and 450 °C in panel (a), and panel (b) presents the UV-Vis spectra of those samples. Not only the colour was not suitable for the TiO$_2$ scaffold, also the mechanical properties were compromised, and the TiO$_2$ was delaminated after the immersion in an electrolyte.
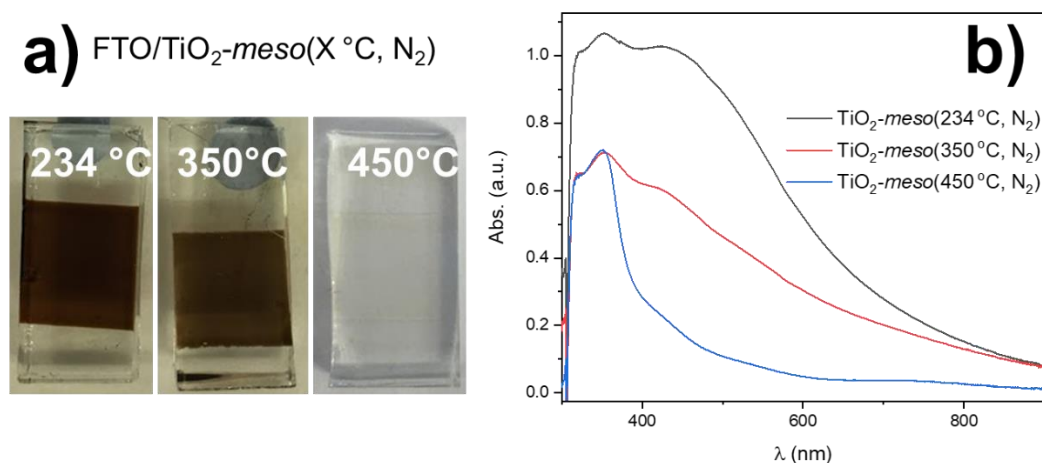

Figure S2.8. (a) Pictures of TiO$_2$-*meso* after N$_2$ annealing at different temperatures 234, 350 and 450 °C for 1 h, (b) UV-Vis spectra of those samples, without prior UV curing.

From figure S2.8, it is evident that only after increasing the temperature upon 450 °C during the N$_2$ annealing, the transparency and mechanical properties of the film were improved. However, at this temperature the stability of the light absorber is compromised. Previously, it has been reported that the interdiffusion at the Sb$_2$Se$_3$/CdS interface hinders light absorption in solar cells following a thermal annealing.[11,12] To assess the stability of this interface after the annealing at 350 °C under N$_2$, a control photoelectrochemical experiment was carried out using Pt as benchmark catalyst for H$_2$ (see section 1.4 of SI for synthetic details). Figure S2.9 shows the light chopped LSV of Sb$_2$Se$_3$/CdS/TiO$_2$/Pt with and without the N$_2$ annealing at 350 °C at 10 mV s^{-1} in 0.1 M H$_2$SO$_4$ with light intensity of 100 mW cm^{-2}

and $\lambda > 340$ nm. It was found that the photocurrent increased followed the annealing demonstrating that the Sb_2Se_3 absorber can tolerate these conditions. Furthermore, the increase in photocurrent is likely associated to the improvement in crystallinity of the RF magnetron sputtered TiO_2 layer after the N_2 annealing as shown before in figure S2.2.[13,14]
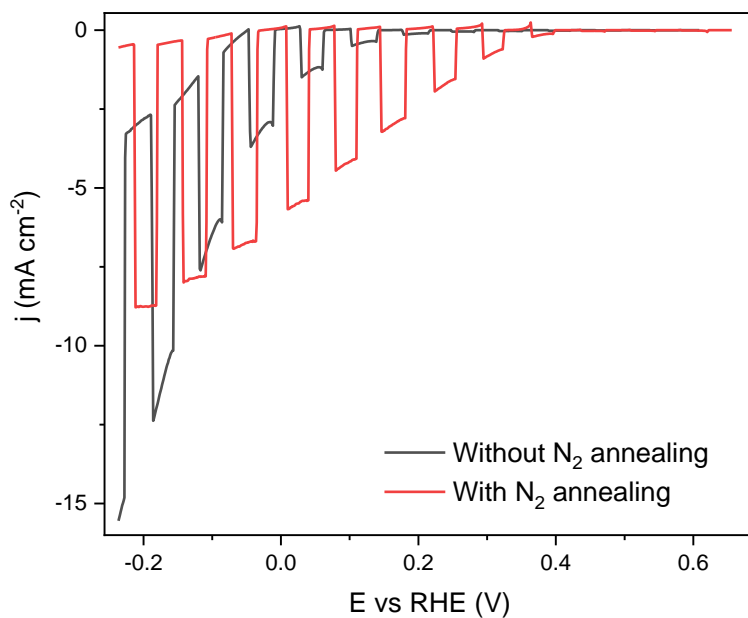

Figure S2.9: Light chopped LSV of Sb_2Se_3/CdS/TiO_2/Pt with and without N_2 annealing at 350 °C for 1 h in 0.1 M H_2SO_4 at 100 mW cm^{-2} and $\lambda > 340$ nm.

Figure S2.10. (a) Cross-sectional SEM image of Sb₂Se₃/CdS/TiO₂-*meso* and EDX maps of Ti, O, Sn, Se, Sb, Si. Note that, since the thickness of Au and CdS layers are 70 nm and 20 nm, it was not possible to detect them.

2.11. Top view EDX analysis of NiP on Sb₂Se₃/CdS/TiO₂-*meso*
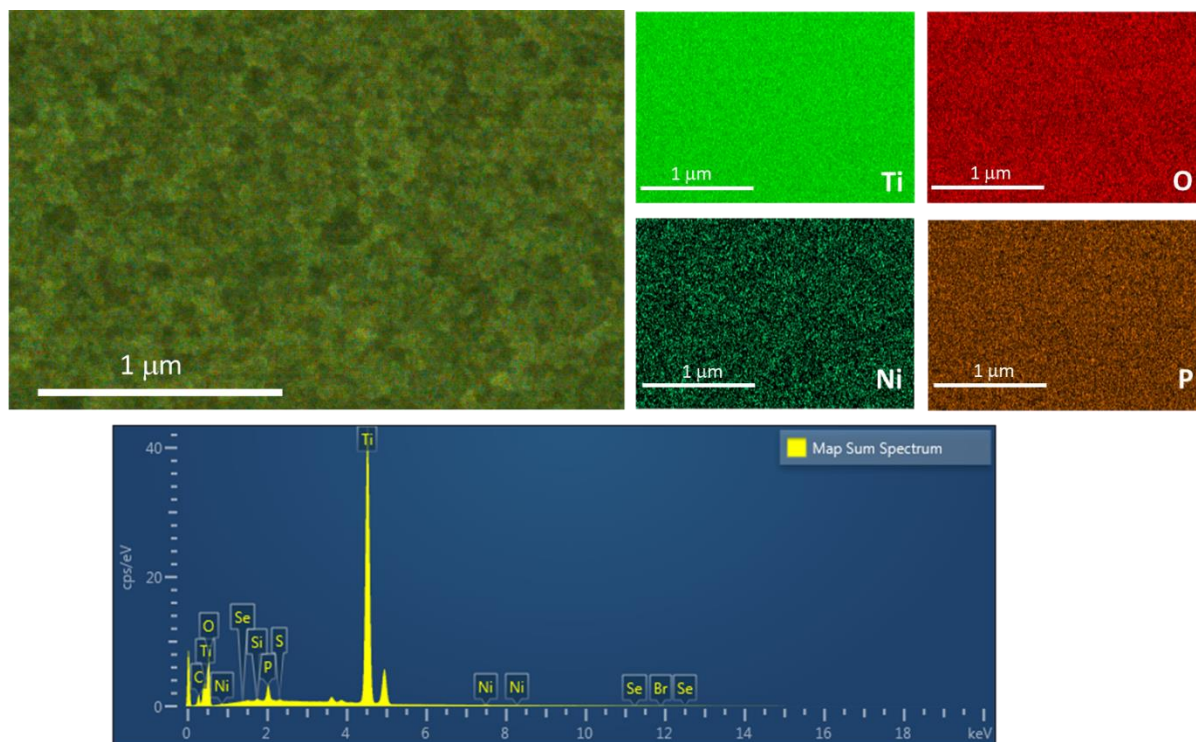
Figure S2.11 Top view EDX analysis of the **NiP** dispersion on the top of Sb₂Se₃/CdS/TiO₂-*meso*, Ni is represented in green, and P is brown.

Figure S12. IPCE
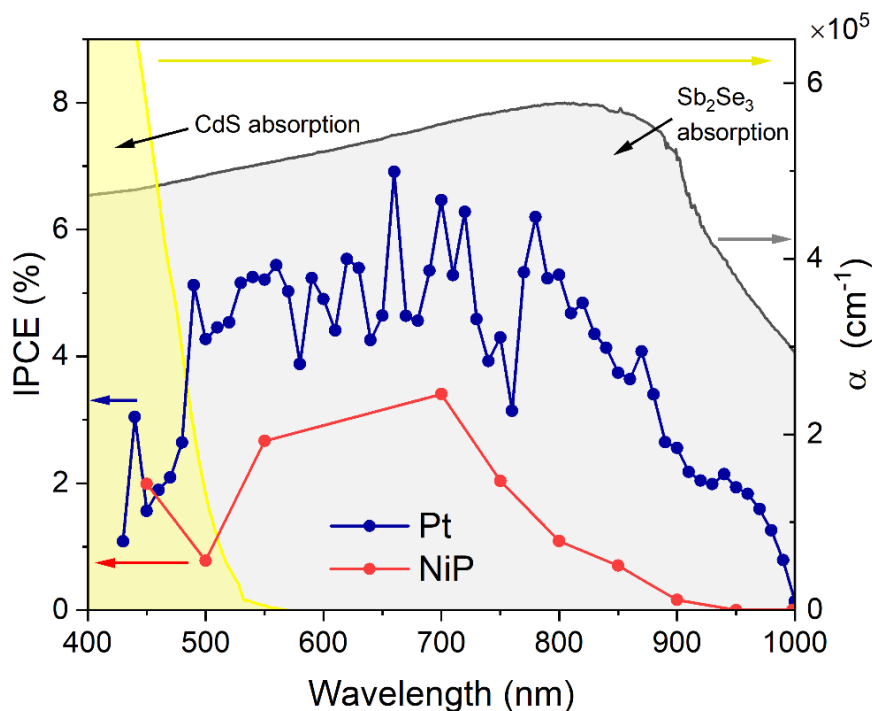
Figure S2.12. IPCE of Sb_2Se_3/CdS/TiO_2-*meso*/**NiP** (red trace) and Sb_2Se_3/CdS/TiO_2-*meso*/Pt (blue trace) at 0 V *vs* RHE in 0.1M Na_2SO_4 pH 3. Overlaid is the absorption spectra of the CdS and Sb_2Se_3 layers.

The IPCE responses show that the activity is significantly decreased at $\lambda < 500$ nm. This wavelength corresponds to the onset of light absorption by the CdS layer suggesting that photon absorption in this layer is not leading to useful photoelectron generation and that parasitic photon absorption occurs.

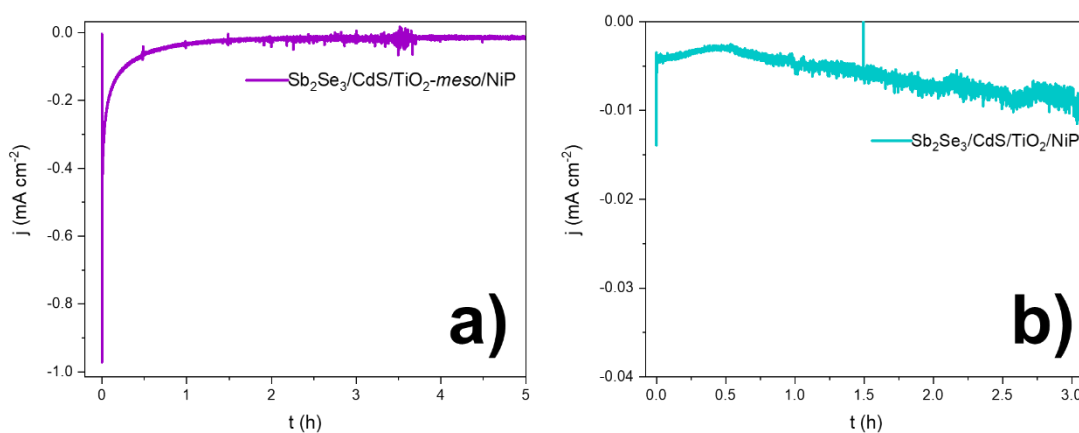**2.13 H_2 production over 5h CPP with the complete device**

Figure S2.13 Controlled Potential Photoelectrolysis at 0 V *vs* RHE of Sb_2Se_3/CdS/TiO_2(-*meso*)/**NiP** with (a) and without (b) the TiO_2-*meso* layer in 0.1M Na_2SO_4 pH 3 at 100 mW cm^{-2} and $\lambda > 340$nm.
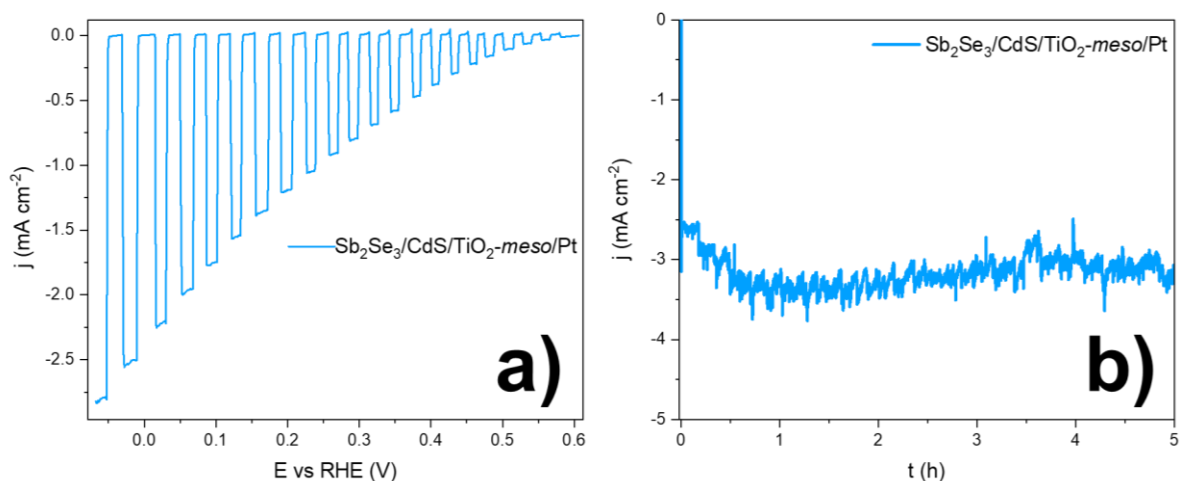
S14. Sb₂Se₃/CdS/TiO₂-*meso*/Pt

Figure S14: (a) Light chopped LSV of Sb₂Se₃/CdS/TiO₂-*meso*/Pt at 10mV s⁻¹, and (b) CPP at 0 V *vs* RHE in 0.1M Na₂SO₄ pH 3 at 100 mW cm⁻² and λ > 340 nm.
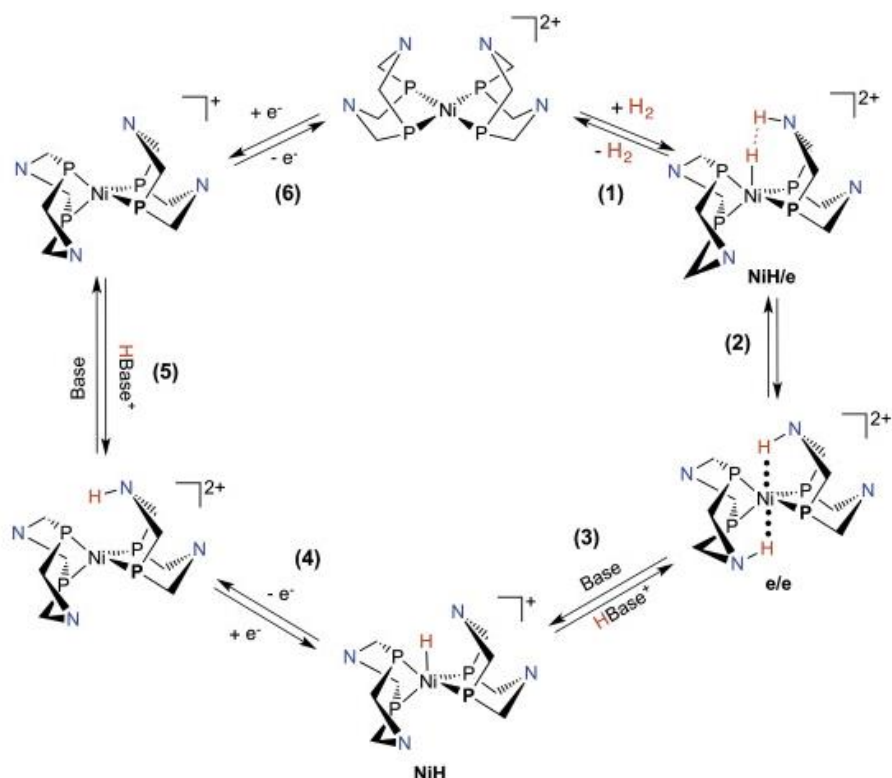
2.15 NiP reaction mechanism

Figure S2.15. NiP reaction mechanism for H₂ production (anti-clockwise).[15] Only the NiP core ([Ni(P₂^{R'}N₂^{R''})₂]²⁺) is shown and the R and R' substituents are omitted for clarity. (P₂^{R'}N₂^{R''} = bis(1,5-R'-diphospha-3,7-R''-diazacyclooctane).
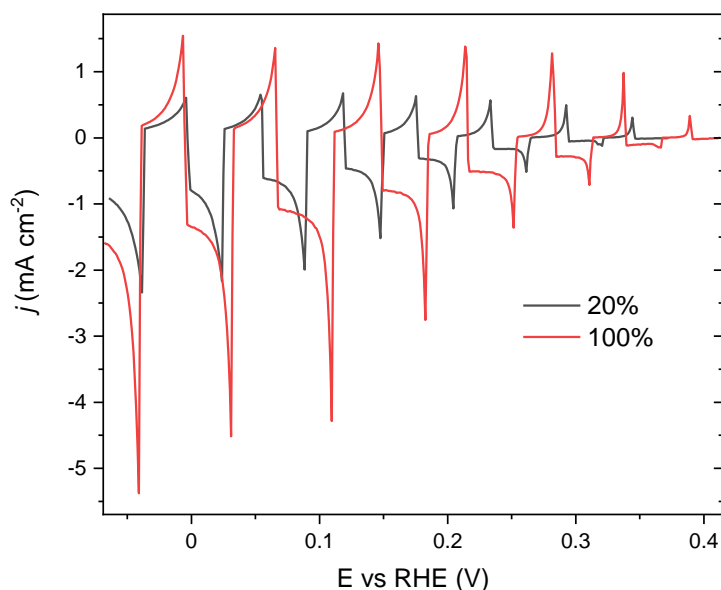
2.16 LSV at 20% light intensity

Figure S2.16: Chopped light LSV of Sb_2Se_3/CdS/TiO_2-*meso*/**NiP** at 10 mV s^{-1} at 20 mW cm^{-2} (20%, black) and 100 mW cm^{-2} (100%, red) in 0.1 M Na_2SO_4 pH 3, and λ > 340nm. Lowering the light intensity by using neutral density filters from 100 to 20 mW cm^{-2} leads to a smaller percentage decrease in photocurrent (from 1.30 to 0.81 mA cm^{-2} at 0 V *vs* RHE, ca. 38%) than the percentage change in light intensity (80% decrease) with FTO/Au/Sb_2Se_3/CdS/TiO_2/TiO_2-*meso*/**NiP**.

2.17 CPP at 20% light intensity
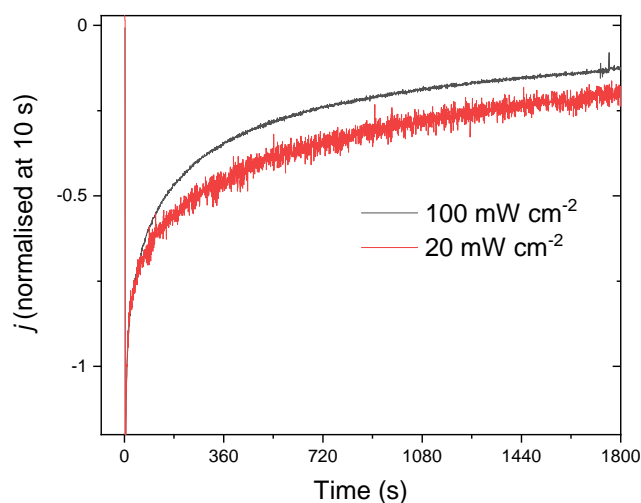
Figure S2.17. Normalised CPP at 0 V *vs* RHE of Sb_2Se_3/CdS/TiO_2-*meso*/**NiP** at 20 mW cm^{-2} (red) and 100 mW cm^{-2} (black) in 0.1M Na_2SO_4 pH 3. The lower light intensity also increases the stability with 20% of photocurrent being retained after 1800 s of operation when 20 mW cm^{-2} is used compared to 11% at 100 mW cm^{-2}.

S18. SEM images after the bulk electrolysis
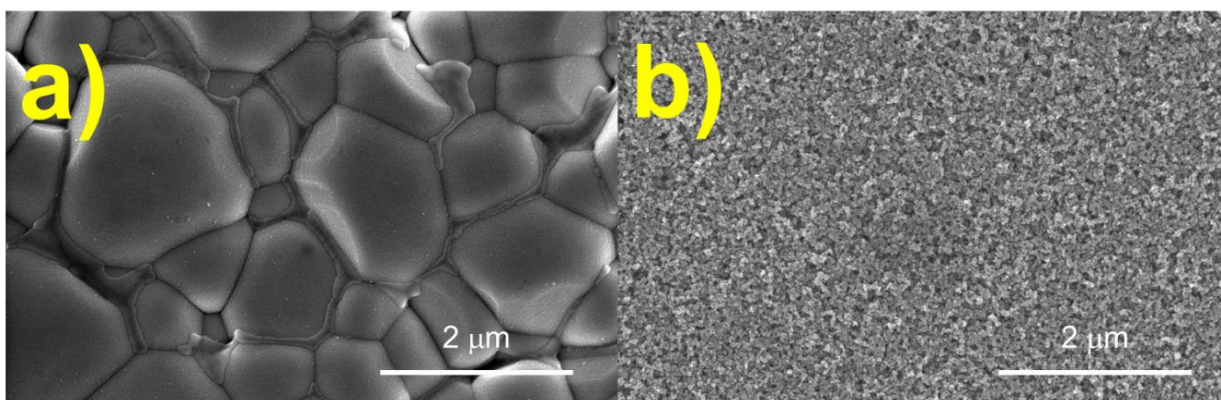
Figure S2.18 Top view SEM images of (a) Sb$_2$Se$_3$/CdS/TiO$_2$/**NiP** and (b) Sb$_2$Se$_3$/CdS/TiO$_2$-*meso*/**NiP** after 5 h of CPP at 0 V *vs* RHE in 0.1M Na$_2$SO$_4$ pH 3 at 100 mW cm^{-2} and λ>340 nm.
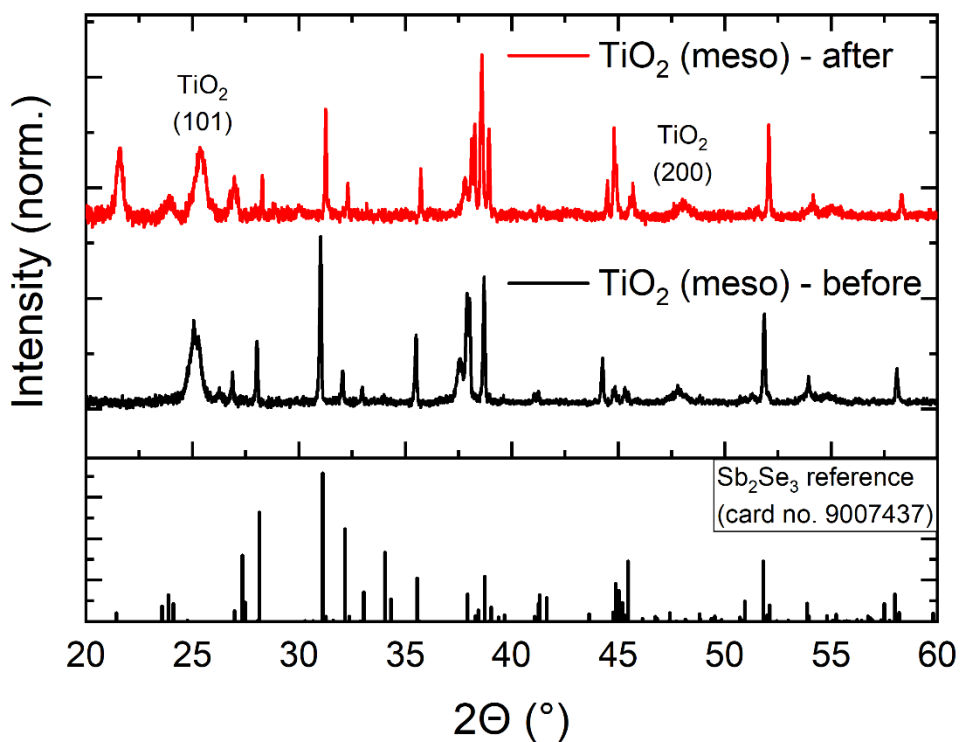
S2.19. XRD

Figure S2.19 XRD pattern of Sb$_2$Se$_3$/CdS/TiO$_2$-*meso*/**NiP** before (black trace) and after (red trace) the CPP test at 0 V *vs* RHE for 5 h.

2.20. Raman spectra after CPP at 0 V *vs* RHE in 0.1M Na₂SO₄ pH 3 for 5 h
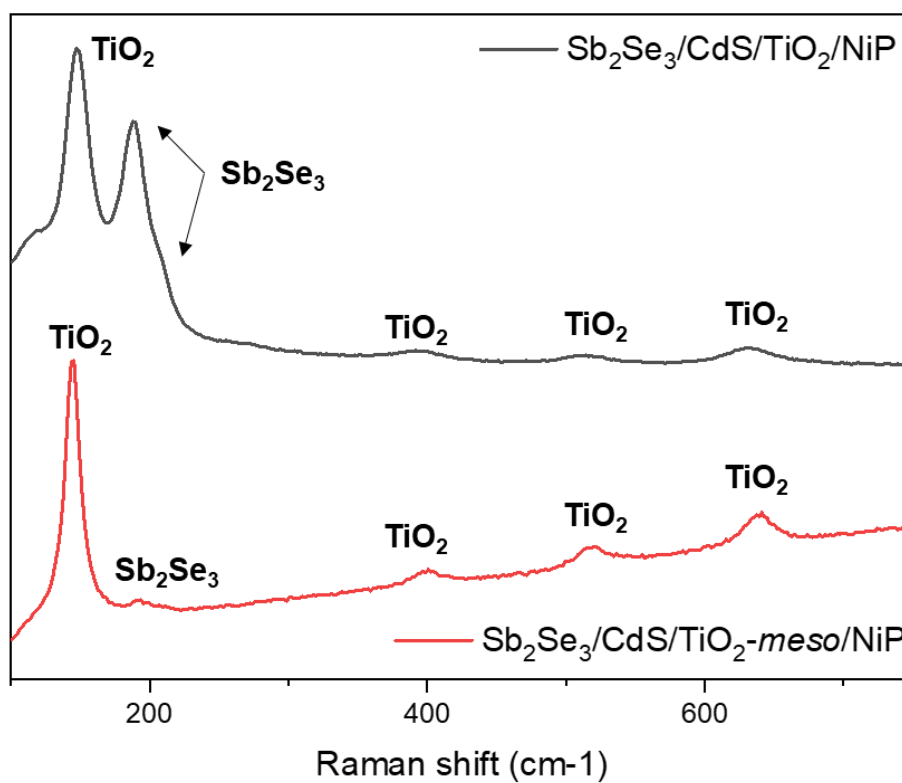
Figure S2.20. Raman spectra after 5 h of CPP at 0 V *vs* RHE on Sb₂Se₃/CdS/TiO₂/**NiP** (black trace) and Sb₂Se₃/CdS/TiO₂-*meso*/**NiP** (red trace) in 0.1M Na₂SO₄ pH 3 at 100 mW cm⁻² and λ > 340 nm.

S21. Light chopped LSV of Sb₂Se₃/CdS/TiO₂-*meso*/Pt previously used with NiP as H₂ catalyst.
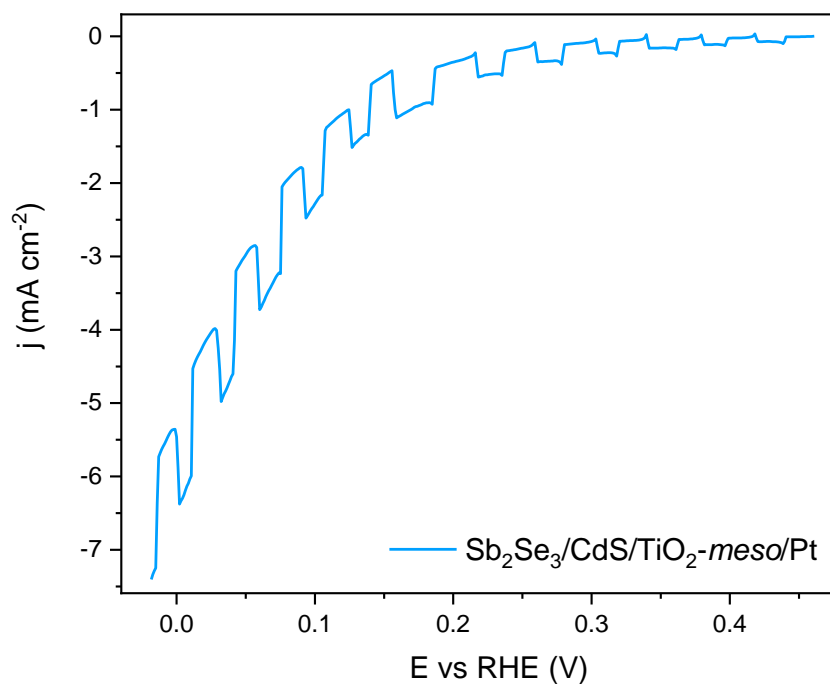
Figure S2.21. Light chopped LSV of Sb$_2$Se$_3$/CdS/TiO$_2$-*meso*/Pt at 10 mV s^{-1} in 0.1 M Na$_2$SO$_4$ pH 3 at 100 mW cm^{-2} and λ > 340 nm. For these experiments, **NiP** was used first as H$_2$ catalyst and went through light chopped LSV at 10 mV s^{-1} and the CPP test at 0 V *vs* RHE for 1 h in 0.1 M Na$_2$SO$_4$ pH 3 at 100 mW cm^{-2} and λ > 340 nm, then **NiP** was stripped in 0.1 M NaOH from the electrode surface followed by the platinization of the sample.

Supporting tables

Table S1. NiP molecular catalyst loading.

Sample	NiP [nmol cm^{-2}]
TiO$_2$-*meso* (UV, 350°C N$_2$)	37.36 ± 9.03
TiO$_2$-*meso* (450°C, air)	39.04 ± 8.36
Sb$_2$Se$_3$/CdS/TiO$_2$/**NiP**	7.08 ± 0.43
Sb$_2$Se$_3$/CdS/TiO$_2$-*meso*/**NiP**	45.76 ± 0.81

Table S2. XPS peak position of NiP catalyst pre and post CPP test for 5 h at 0 V *vs* RHE in 0.1M Na$_2$SO$_4$ pH 3 at 100 mW cm^{-2} and λ > 340 nm.

Hybrid photoelectrode	CPP	N (1s)	P (2p)	Ni (2p 1/2)	Ni (2p 3/2)	Ref.
p-Si/TiO$_2$/**NiP**	pre	399.6	132.5	872	854.8	4
	post	400.2	132		854.8	
FTO/TiO$_2$/**NiP**	pre	396.4	129.4	868.9	851.5	8
	post	396.2	129	869.1	851.5	
Au/La$_5$Ti$_2$Cu$_{0.9}$Ag$_{0.1}$S$_5$O$_7$/TiO$_2$/**NiP**	pre	398.67	132.5	860.4	855	5
	post	400.2	132.5	na	na	
Sb$_2$Se$_3$/CdS/TiO$_2$-*meso*/**NiP**	pre	399.6	132.6	872.1	854.6	This work
	post	399.8	134.3	na	na	
	NiP	399.5	133.1	872	854.8	

Table S3. Hybrid photocathodes for H$_2$ production.

Photocathode	j (mA cm^{-2}) @ 0 V vs RHE	Stability (%) t (h)	Electrolyte	Light source	Ref.
p-Si/TiO$_2$/**NiP**	0.35	28% 24	0.1 M Acetic Acid pH 4.5	AM 1.5G, 100 mW cm^{-2} λ> 400 nm	4
Au/LTCA/TiO$_2$/**NiP** LTCA: La$_5$Ti$_2$Cu$_{0.9}$Ag$_{0.1}$S$_5$O$_7$	0.5	8% 6	0.1 M Na$_2$SO$_4$ pH 3	AM 1.5G, 100 mW cm^{-2}	5
*FTO/TiO$_2$/**NiP**	0.2	25% 8	0.1 M Na$_2$SO$_4$ pH 3	*	8
Sb$_2$Se$_3$/CdS/TiO$_2$-*meso*/**NiP**	1.3	3% 1	0.1 M Na$_2$SO$_4$ pH 3	100 mW cm^{-2} λ> 340 nm	This work
Sb$_2$Se$_3$/CdS/TiO$_2$-*meso*/NiP	0.8	20% 0.5	0.1 M Na$_2$SO$_4$ pH 3	20 mW cm^{-2} λ> 340 nm	This work
p-Si/ALD-TiO$_2$/SC-TiO$_2$/**Co$_{C11P}$**/ALD-TiO$_2$	1.3	77% 1	1 M PBS pH 7	AM 1.5G, 100 mW.cm^{-2}	16

p-Si/TiO$_{2(ALD/DB)}$/**Ni(N$_5$)^{HA}**	1	100%	0.1 M PBS pH 7	AM 1.5G, 100 mW cm^{-2}	17
p-Si/TiO$_{2(ALD/DB)}$/**Co(N$_5$)^{HA}**	0.7	100%	0.1 M PBS pH 7	AM 1.5G, 100 mW cm^{-2}	17
p-Si/TiO$_{2(ALD/DB)}$/**CoPy^{HA}**	0.4	84% 6	0.1 M PBS pH 7	AM 1.5G, 100 mW cm^{-2}	17
Si/TiO$_2$/**Co(CR-DCP)**	0.68	100% 10	0.1 M ABS pH 4.5	AM 1.5G, 100 mW cm^{-2} λ> 400 nm	18
CuFe$_x$O$_y$/TiO$_2$/**CoHEC**	4.5 0.4 V vs RHE	67% 20 min	0.2 M PBS pH 6.7	1 sun visible light (400–780 nm)	19
p-Si/TiO$_2$/**CoPy-4-CONH(OH)**	0.319	≈100% 2	0.1 M BBS pH 9	AM 1.5G, 100 mW cm^{-2} λ> 400 nm	20
p-Si/TiO$_2$/**CoPy-4-PO$_3$H$_2$**	0.18	75% 2	0.1 M BBS pH 9	AM 1.5G, 100 mW cm^{-2} λ> 400 nm	20
p-Si/TiO$_2$/**CoPy-4-COOH**	0.158	66% 2	0.1 M BBS pH 9	AM 1.5G, 100 mW cm^{-2} λ> 400 nm	20
GaInP$_2$/TiO$_2$/**(OOCpy)Co(dmgH)$_2$(Cl)**/TiO$_2$	9	56% 20	0.1M NaOH pH 13	1-sun illumination 100 mW cm^{-2}	21

*This study did not used a light absorber, instead a potential of -0.25 V vs RHE was applied. SC- Spin coating, ALD-Atomic Layer Deposition, DB-Doctor-blading, ABS: Acetic buffer solution, PBS: Phosphate buffer solution, BBS: Borate buffer solution

Table S3 compares the PEC performance of hybrid photocathodes using **NiP** molecular catalyst. The stability was defined as the photocurrent measured at the beginning of the CPP (J_0 @ $t = 0$) against the photocurrent measured at certain time (J @ t (h)) at 0 V vs RHE, according to (2).

$$\% \, Stability = \frac{J \, @ \, t \, (h)}{J_0 \, @ \, t=0} \qquad (2)$$

Supporting References

1   O. S. Hutter, L. J. Phillips, K. Durose and J. D. Major, *Sol. Energy Mater. Sol. Cells*, 2018, **188**, 177–181.

2   W. Yang, J. H. Kim, O. S. Hutter, L. J. Phillips, J. Tan, J. Park, H. Lee, J. D. Major, J. S. Lee and J. Moon, *Nat. Commun.*, 2020, **11**, 1–10.

3   M. A. Gross, A. Reynal, J. R. Durrant and E. Reisner, *J. Am. Chem. Soc.*, 2014, **136**, 356–366.

4   J. J. Leung, J. Warnan, D. H. Nam, J. Z. Zhang, J. Willkomm and E. Reisner, *Chem. Sci.*, 2017, **8**, 5172–5180.

5   T. E. Rosser, T. Hisatomi, S. Sun, D. Antón-García, T. Minegishi, E. Reisner and K. Domen, *Chem. Eur. J.*, 2018, **24**, 18393–18397.

6   M. L. Helm, M. P. Stewart, R. M. Bullock, M. R. DuBois and D. L. DuBois, *Science*, 2011, **333**, 863–866.

7   J. Tauc, R. Grigorovici and A. Vancu, *Phys. Status Solidi B*, 1966, **15,** 627-637.

8   T. E. Rosser, M. A. Gross, Y. H. Lai, E. Reisner, B. C. M. Martindale, G. A. M. Hutton, C. A. Caputo, E. Reisner, M. A. Gross, A. Reynal, J. R. Durrant, E. Reisner, J. J. Leung, J. Warnan, D. H. Nam, J. Z. Zhang, J. Willkomm and E. Reisner, *Chem. Sci.*, 2016, **7**, 4024–4035.

9   R. R. Prabhakar, W. Septina, S. Siol, T. Moehl, R. Wick-Joliat and S. D. Tilley, *J. Mater. Chem. A Mater.*, 2017, **5**, 23139–23145.

10 D. R. Lide and G. W. A. Milne, *Handbook of Data on Organic Compounds*, CRC Press, Florida, 3rd edn., 1993.

11 H. Shiel, O. S. Hutter, L. J. Phillips, J. E. N. Swallow, L. A. H. Jones, T. J. Featherstone, M. J. Smiles, P. K. Thakur, T. L. Lee, V. R. Dhanak, J. D. Major and T. D. Veal, *ACS Appl. Energy Mater.*, 2020, **3**, 11617–11626.

12 R. E. Williams, Q. M. Ramasse, K. P. McKenna, L. J. Phillips, P. J. Yates, O. S. Hutter, K. Durose, J. D. Major and B. G. Mendis, *ACS Appl. Mater. Interfaces*, 2020, **12**, 21730–21738.

13 A. Paracchino, N. Mathews, T. Hisatomi, M. Stefik, S. D. Tilley and M. Grätzel, *Energy Environ. Sci.*, 2012, **5**, 8673–8681.

14 A. Paracchino, V. Laporte, K. Sivula, M. Grätzel and E. Thimsen, *Nat. Mater.*, 2011, **10**, 456–461.

15 W. J. Shaw, M. L. Helm and D. L. du Bois, Biochim. *Biophys. Acta Bioenerg.*, 2013, **1827**, 1123–1139.

16 S. Chandrasekaran, N. Kaeffer, L. Cagnon, D. Aldakov, J. Fize, G. Nonglaton, F. Baleras, P. Mailley and V. Artero, *Chem. Sci.*, 2019, **10**, 4469–4475.

17 L. Gong, P. Zhang, G. Liu, Y. Shan and M. Wang, *J. Mater. Chem. A Mater.*, 2021, **9**, 12140–12151.

18 C. Nie, C. Liu, L. Gong and M. Wang, *J. Mater. Chem. A Mater.*, 2021, **9**, 234–238.

19 C. Tapia, E. Bellet-Amalric, D. Aldakov, F. Boudoire, K. Sivula, L. Cagnon and V. Artero, *Green Chem.*, 2020, **22**, 3141–3149.

20 L. Gong, H. Yin, C. Nie, X. Sun, X. Wang and M. Wang, *ACS Appl. Mater. Interfaces*, 2019, **11**, 34010−34019.

21   J. Gu, Y. Yan, J. L. Young, K. X. Steirer, N. R. Neale and J. A. Turner, *Nat. Mater.*, 2016, **15**, 456–462.